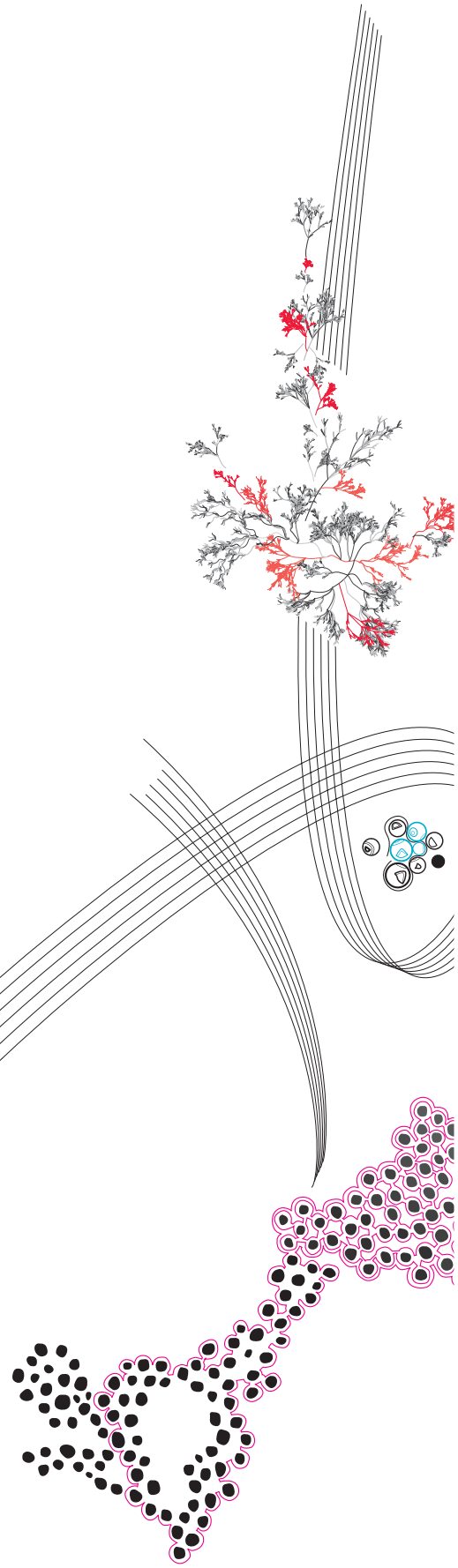

BSc Thesis Applied Mathematics & Applied Physics

Blood flow simulation in carotid arteries with computational fluid dynamics

Ties Hidde Martens

Supervisors:
J.M. Suk,
G.P.R. Lajoinie,
J.M. Wolterink

July, 2022

Department of Applied Mathematics
Faculty of Electrical Engineering,
Mathematics and Computer Science &
Afdeling Technische Natuurkunde
Faculteit van Technische
Natuurwetenschappen

UNIVERSITY OF TWENTE.

Blood flow in carotid arteries simulated by computational fluid dynamics

T. H. Martens

July, 2022

Abstract

Hemodynamic quantities like wall shear stress (WSS) and blood pressure in the carotid arteries have been found to correlate with plaque development and arterial remodelling which could result in atherosclerosis, which is one of the leading causes for ischemic strokes. Computational fluid dynamics (CFD) is a tool that can be used to simulate blood flow inside arteries and from there these hemodynamic quantities can be calculated. In this work, data generated from applying a segmentation algorithm on MRI-scans of carotid arteries in a patient is used to construct a 3D tetrahedral finite element mesh of the lumen wall of the artery. The incompressible Navier Stokes equations are solved inside the mesh to get a steady state velocity and pressure profile over the artery. Using this flow profile, clinically relevant biomarkers can be found. This research therefore provides a general way of finding blood flow inside MRI-derived carotid artery segmentations.

Keywords: Carotid blood flow, Computational fluid dynamics, Surface mesh generation, Volume mesh generation

1 Introduction

Plaque development in carotid arteries can be the cause of atherosclerosis, which reduces blood flow towards the brain. Atherosclerosis in major intra and extracranial arteries like the carotid arteries is one of the most common causes of stroke [5, 25]. Hemodynamic quantities like wall shear stress (WSS) and blood pressure were found to correlate with atherosclerotic plaque development [20, 18]. Both WSS and blood pressure can be determined from the blood flow inside the artery.

Several techniques exist for measuring blood flow in major arteries. However, measuring blood flow using a catheter has its complications and risks [19]. Therefore, noninvasive methods are preferable to reduce the medical complications. A noninvasive method like particle image velocimetry becomes inaccurate in regions of low WSS [6] and 4D flow MRI fails to provide blood flow descriptions that are sufficiently accurate to be of direct clinical value[23].

Another noninvasive approach uses MRI angiography in sequence with a segmentation procedure, to create a 3D finite element mesh employing mesh construction algorithms. If this mesh is sufficiently refined, the Navier Stokes equations can be solved repeatedly over time using computational fluid dynamics (CFD). This process will lead to a model of the 3D velocity profile of the blood flow through the artery along with the scalar pressure throughout the blood vessel. From these two parameters, clinically relevant biomarkers can be readily determined. Methods similar to this were already applied to determine the fractional flow reserve (FFR) inside coronary arteries [30].

The advantage of this method is that it is noninvasive and therefore it will decrease the amount of surgical complications that could arise. It is also not subject to all kinds of systematic errors that would arise when invasive methods are used. For example, for the catheterization method, the presence of a catheter inside an artery will influence the blood flow.
If this method leads to robust blood flow models, then it could be generally applied to segmentations of MRI-scans of carotid arteries, providing a solid method to calculate patient specific hemodynamic quantities.
Additionally, once a numerically converging model of the blood flow is made, this data can be used as ground truth to a graph convolutional network which would be able to produce fast and accurate estimations of biomarkers like WSS[29].

2 Theory

To estimate blood flow in blood vessel shapes from MRI-scans, four steps are taken. Firstly, a tetrahedral finite element mesh is created from a point cloud that was obtained from a segmentation algorithm applied to a medical image. To be able to find a weak solution to the incompressible Navier-Stokes equations, they are transformed to a sequence of three linear variational forms. To compute blood flow, a set of three Dirichlet boundary conditions are imposed on the mesh. Finally, a high performance computer is used to find a solution to the equations using linear system solvers. The following sections will describe these steps in more detail.

2.1 Meshing algorithms

The carotid arteries are a set of two common carotid arteries that each bifurcate into an external carotid artery and an internal carotid artery. The carotid arteries can thus be described as four branches. In an effort to decrease the complexity of the problem, the upstream and the downstream vasculature is modelled by inflow and outflow boundary conditions.

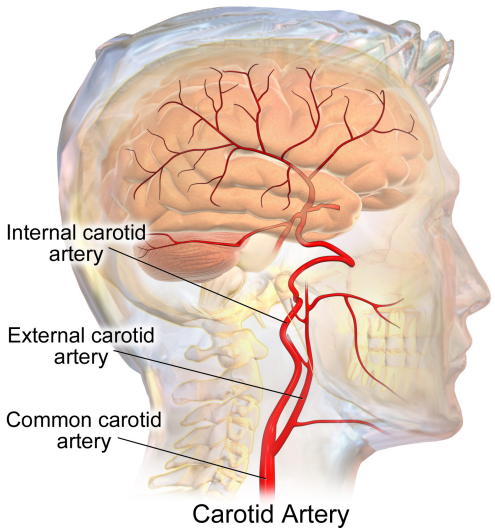

FIGURE 1: The right common carotid artery bifurcates into the external and internal carotid arteries [28].

The starting point for creating the mesh is data that is obtained from applying a segmentation algorithm on the medical imaging data [1]. This data consists of four point clouds for each patient, which geometrically describe the lumen wall of the left and right external carotid artery as well as the left and right internal carotid arteries. A point cloud is saved as a collection of level sets, stacked on top of each other along the z-axis. Every level set contains a number of vertices described in Cartesian coordinates. The vertices are ordered clockwise at a constant angle interval. Inside each level set, an interpolation is made through the vertices, connecting them with a smooth B-spline loop. Then, 48 equally spaced vertices are created along each loop (Figure 2).

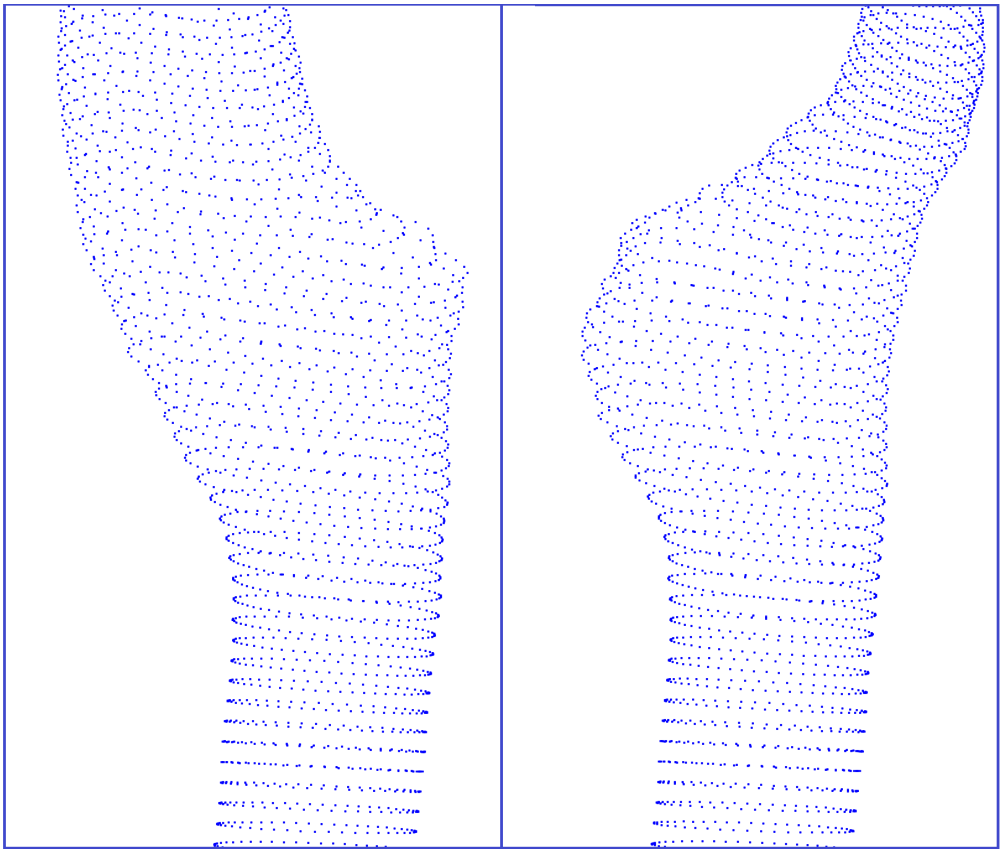

FIGURE 2: The segmented imaging data from the right external carotid artery is transformed to a collection of level sets, each level set consisting of 48 vertices.

Next is the creation of a triangular surface mesh that describes the entire part of the lumen wall of the artery that we are interested in. The mesh is defined as (V, F), where V is a set of vertices and F is a set of faces. A face is defined as an ordered tuple of 3 vertices which induce a face normal dependent on the ordering of the vertices. The orientation of the face normal is determined by the left hand rule. To create the appropriate faces, a vertex v_0 is linked by an edge to its clockwise neighbour v_1 inside the same level set, after which v_0 and v_1 are both linked by an edge to the vertex v_{48} closest to v_0 inside an adjacent level set. In this way the first face is defined as $F_1 = (v_0, v_1, v_{48})$. Triangular polygons are created throughout the entire point cloud in this way such that the resulting mesh is watertight everywhere except at the in and outlets of the model.

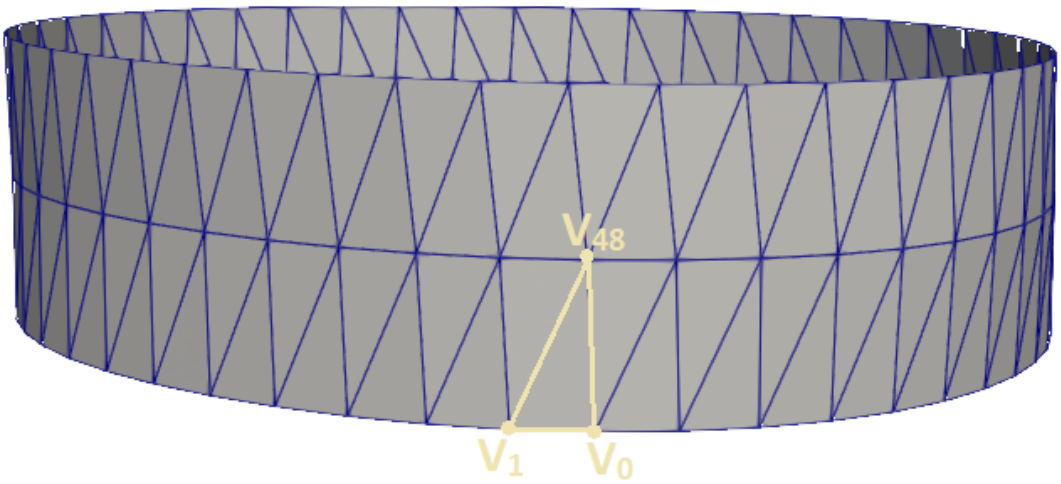

FIGURE 3: The initial surface mesh is created by interconnecting vertices from adjacent level sets.

The segmentation algorithm's predictive uncertainty in the position of the data from the segmentation increases towards both ends of the vessel. This is due to the fact that the image quality of the MRI-scan is more noisy in these parts. As including all data would lead to extremely noisy meshes towards either end of the vessel, only the part where the uncertainty in the position is relatively small is used for the creation of the mesh. The exact collection of level sets that is used is manually selected based on visual inspection of the mesh.

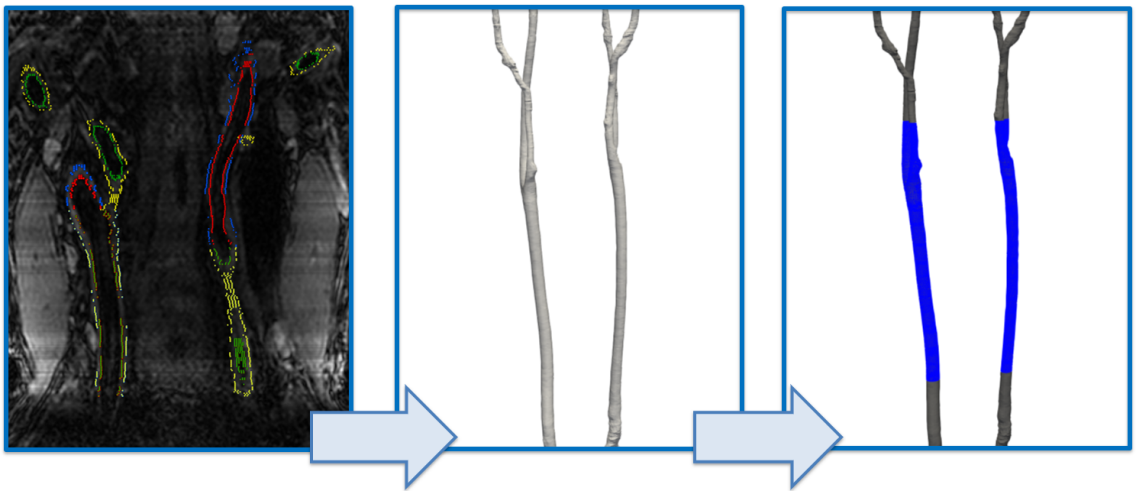

FIGURE 4: From the segmented imaging data, a simple surface mesh is created. As the uncertainty in the position of the vessel wall at both ends of the vessel increases, only a certain part of the vessel is used for simulation.

In order to simulate the blood flow through the bifurcation of the common carotid artery, the meshes of the left and right carotid artery are to be merged. To merge the meshes we use a boolean union algorithm based on the enclosed volume of both meshes. However, as the meshes are not watertight, they do not enclose any volume. Hence, a

simple surface mesh is generated for the entrance and the exits of the vessel by simply interconnecting vertices in the lowest and highest level sets, as can be seen in Figure 5(left). Now, the mesh contains no more cavities. Another necessity for a surface mesh to enclose a volume is that the normal vectors of all faces point either outwards or inwards of the mesh. Since the normal vector of a face is induced by the ordering of vertices, and the faces were not constructed in a way that the normal vector is consistently pointing outwards or inwards, this needs to be changed. A mesh repair algorithm developed by Trimesh [9] redefines the faces by ordering the vertices inside them differently. After application of this algorithm, all face normals point outwards and the meshes are watertight and ready to be merged.

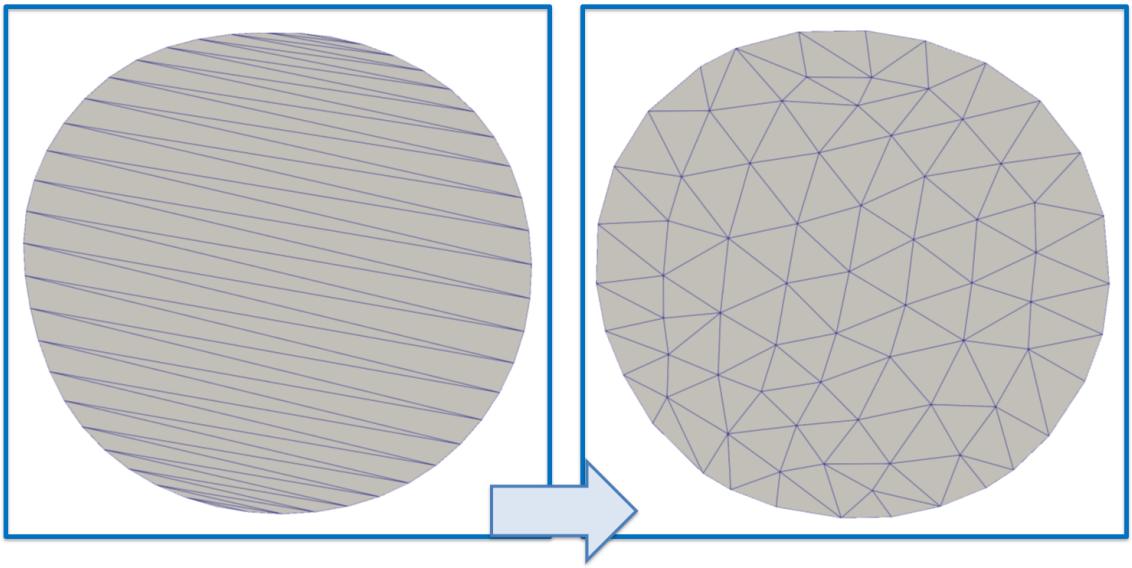

FIGURE 5: The entrance and exits of the blood vessel are connected in a trivial way to make the mesh watertight (left), and are then smoothened after isotropic remeshing of the 2D surface mesh (right).

After the surface meshes are closed by the entrance and exits, the mesh of the external and internal carotid artery can be merged. Let V_{ext} and V_{int} denote the volumes enclosed by the surface meshes of the external and internal carotid artery respectively. The boolean merging algorithm of Meshlab [8] calculates the merged volume:

$$V_{merged} = \{x | x \in (V_{ext} \cup V_{int})\}.$$

The result of the merging algorithm is a new mesh that exactly encloses the volume V_{merged}. After the meshes have been merged, the resulting mesh has some areas in which a lot of small faces have been created, especially close to the bifurcation (see Figure 6. This is due to the fact that the merging algorithm takes exactly the area that it is supposed to enclose. This level of refinement is not necessary for the simulation, and this could lead to an unnecessary amount of calculation for the linear solver to compute. Additionally, 'badly shaped' polygons like the ones at the intersection of the merging have been found empirically to introduce artifacts in the CFD simulation results [7]. Therefore, an isotropic smoothing algorithm from Meshlab is applied.

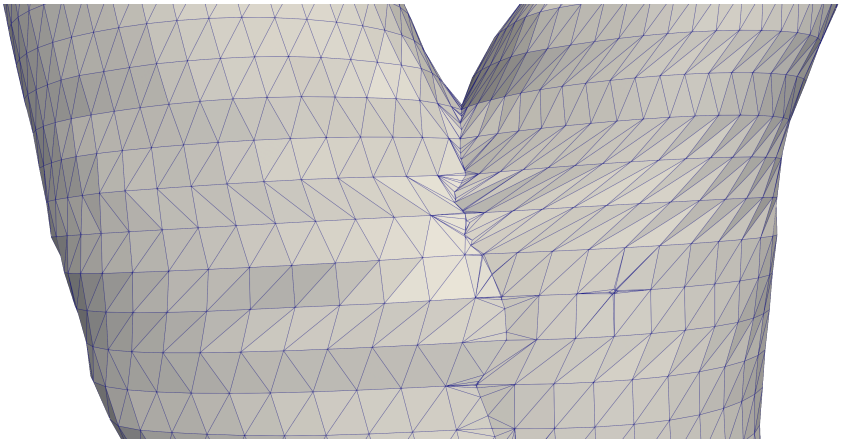

FIGURE 6: After merging the two meshes, the mesh becomes very refined close to the bifurcation. Additionally, 'badly shaped' triangles can be seen especially to the right of the bifurcation as they are stretched to long.

Isotropic remeshing is an algorithm that repeatedly applies edge flip, collapse, relax and refine operations on a triangular mesh to regularize the size of all triangles in the mesh. After three iterations of these operations the faces of the mesh are more similar in size and the bifurcation is no longer overly refined.

Then the quality of the mesh is improved by using the mesh adaptation algorithm created by open-source software mmg [4]. This moves the vertices inside the 2D manifold by a sequence of algorithms that optimises heuristically defined quality metrics.
The last step in the mesh creation process is to convert the surface mesh to a tetrahedral volume mesh. For this a Delaunay tetrahedralization process is applied to the surface mesh that fills the volume that is enclosed by the mesh with tetrahedral elements. This process is done using a software package called TetGen [27].

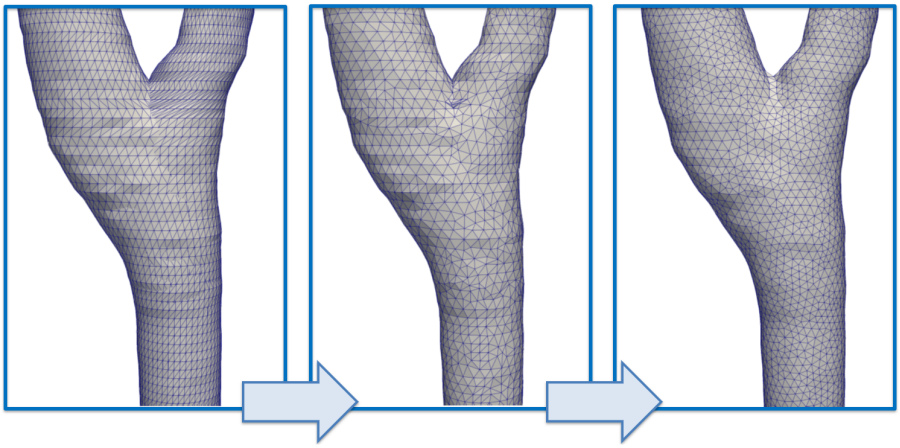

FIGURE 7: The surface meshes of two branches of the carotid artery are merged and smoothed to create a single volumetric mesh.

Alternative methods for creating a mesh from a point cloud include Poisson surface reconstruction [16] which could potentially result in a mesh shape that is closer to the actual blood vessel shape, or implicit geometric regularization [15] which is uses neural networks that represent shapes as level sets of data.

2.2 Navier Stokes equations

After a finite element mesh for the simulation has been created, blood flow will be simulated inside this mesh. The first simplification that is made is the 'rigid wall' assumption. The lumen wall of the artery is elastic and its shape is dependent on parameters like the wall thickness and blood pressure[22]. For simplicity however, in this study the lumen wall of the artery is considered to be a rigid wall that does not change in shape. The second simplification can be made for medium to large sized arteries, e.g. the main branch of the aorta and the carotid arteries [32]. Blood flow inside these arteries can be considered incompressible, meaning that the density and volume of the blood do not change with pressure. Therefore the blood flow is modelled by solving the incompressible Navier Stokes equations:

$$\rho(\frac{\partial u}{\partial t} + u \cdot \nabla u) = \nabla \cdot \sigma(u, p) + f, \tag{1a}$$

$$\nabla \cdot u = 0, \tag{1b}$$

where ρ is the density, u is the velocity, σ is the shear stress and p is the pressure. Note that the ∇u represents taking the gradient of u, whereas the $\nabla \cdot \sigma$ represents taking the divergence of σ.

A strong solution to the Navier Stokes equations on general domains is not known. Hence, an alternative approach is taken by solving the weak form of equations (1a) and (1b). The approach followed in this section was inspired by [2]. As the carotid arteries are relatively large blood vessels the blood can be regarded a Newtonian fluid[10], therefore the viscous stresses are at every point linearly correlated to the local strain rate and the stress tensor is given by:

$$\sigma(u, p) = 2\mu\epsilon(u) - pI,$$

with the strain rate is described by:

$$\epsilon(u) = \frac{1}{2}(\nabla u + (\nabla u)^T).$$

No external forces like for example gravity are taken into consideration and consequently in equation (1a), $f = 0$.
As the Navier-Stokes equations in this form are a nonlinear system of equations, they are written in variational form and a multistep technique is used to describe the problem as a sequence of three linear variational problems over time [14].
The first variational problem is obtained by multiplying equation (1a) by a test function v and integrating each term over its domain, where v is a function from a vector valued second order function space. To approximate the derivative of the velocity with respect to time a forward difference scheme is used: $\frac{\mathrm{d}u}{\mathrm{d}t} \approx \frac{u_* - u_n}{\Delta t}$. The problem is to find the tentative velocity (u_*), using u_n and p_n, such that

$$\iiint_\Omega (\rho\frac{u_* - u_n}{\Delta t})v \,\mathrm{d}x\mathrm{d}y\mathrm{d}z + \iiint_\Omega (\rho u_n \cdot \nabla u_n)v \,\mathrm{d}x\mathrm{d}y\mathrm{d}z = \iiint_\Omega (\nabla \cdot \sigma(u_n, p_n))v \,\mathrm{d}x\mathrm{d}y\mathrm{d}z, \tag{2}$$

where the subscript n denotes the current time step.

Green's theorem can be applied to linearize the nonlinear parts of the equation. Using the assumption that the velocity close to the boundary goes towards zero and the fact that the flow is fully developed, i.e. the derivative of the velocity in the direction of the vessel at the outflow vanishes we get

$$-\iiint_\Omega (\nabla \cdot \sigma(u_n, p_n))v \ \mathrm{d}x\mathrm{d}y\mathrm{d}z = -\iiint_\Omega (\nabla \cdot (\mu(\nabla u + (\nabla u)^T) - pI))v \ \mathrm{d}x\mathrm{d}y\mathrm{d}z =$$

$$\iiint_\Omega (\sigma(u_{n+\frac{1}{2}}, p_n)\epsilon(v) \ \mathrm{d}x\mathrm{d}y\mathrm{d}z + \int_{\partial\Omega} (p_n\vec{n})v \, \mathrm{d}s - \int_{\partial\Omega} (\mu\nabla(\frac{u_{n+1}+u_n}{2})\vec{n})v \, \mathrm{d}s. \tag{3}$$

Where $\partial\Omega$ denotes the boundary of Ω and $\vec{n}$ is the normal vector on the boundary. Finally, equation (3) is substituted in equation (2) to get

$$\iiint_\Omega (\rho\frac{u_* - u_n}{\Delta t})v \ \mathrm{d}x\mathrm{d}y\mathrm{d}z + \iiint_\Omega (\rho u_n \cdot \nabla u_n)v \ \mathrm{d}x\mathrm{d}y\mathrm{d}z + \iiint_\Omega (\sigma(u_{n+\frac{1}{2}}, p_n)\epsilon(v) \ \mathrm{d}x\mathrm{d}y\mathrm{d}z + \int_{\partial\Omega} (p_n\vec{n})v \, \mathrm{d}s - \int_{\partial\Omega} (\mu\nabla(\frac{u_{n+1}+u_n}{2})\vec{n})v \, \mathrm{d}s = 0. \tag{4}$$

The tentative velocity u_* is now used to find the pressure on the next time step p_{n+1} in the second variational problem, which is defined as follows. Taking the difference between equation (1a) with u_* and p_n and the same equation using u_{n+1} and p_{n+1}, results in the following equation:

$$\frac{u_{n+1} - u_*}{\Delta t} + \nabla p_{n+1} - \nabla p_n = 0. \tag{5}$$

The divergence is taken on both sides of equation (5):

$$\frac{1}{\Delta t}(\nabla \cdot u_{n+1} - \nabla \cdot u_*) + \nabla^2 p_{n+1} - \nabla^2 p_n = 0. \tag{6}$$

Then, each term is multiplied by a test function q and integrated over its domain, where q is from a scalar valued first order function space. Using Green's theorem again, along with the fact that $\nabla \cdot u_{n+1} = 0$ from equation (1b) leads to

$$\iiint_\Omega \nabla p_{n+1} \nabla q \ \mathrm{d}x\mathrm{d}y\mathrm{d}z = \iiint_\Omega \nabla p_n \nabla q \ \mathrm{d}x\mathrm{d}y\mathrm{d}z - \frac{1}{\Delta t}\iiint_\Omega (\nabla \cdot u_*)q \ \mathrm{d}x\mathrm{d}y\mathrm{d}z. \tag{7}$$

The third variational problem is to find u_{n+1} based on the previous two variational forms. The equation is obtained by multiplying equation 5 by $(\Delta t)v$ and integrating over the domain again.

$$\iiint_\Omega (u_{n+1})v \ \mathrm{d}x\mathrm{d}y\mathrm{d}z = \iiint_\Omega u_* v \ \mathrm{d}x\mathrm{d}y\mathrm{d}z - \Delta t \iiint_\Omega (\nabla(p_{n+1} - p_n) \ \mathrm{d}x\mathrm{d}y\mathrm{d}z. \tag{8}$$

With appropriate boundary and initial conditions, a numerical solution to the incompressible Navier-Stokes equation can be found by solving equations (4), (7) and (8) iteratively over time.

2.3 Boundary and Initial Conditions

The surface of the mesh can roughly be split into four sections, the inlet $\partial\Omega_{in}$, the outlets $\partial\Omega_{out,1}$ and $\partial\Omega_{out,2}$ and the vessel wall $\partial\Omega_{wall}$. To find a solution to the sequence of variational problems described in the previous section, physical boundary conditions are imposed on every section of the surface of the mesh. Based on the previously mentioned 'rigid wall' assumption, the 'no-slip' boundary condition can be imposed on the mesh:

$$\vec{u}(x,y,z) = \vec{0}, \quad \text{for } (x,y,z) \in \partial\Omega_{wall}. \tag{9}$$

The second boundary condition is applied at the inlet of the vessel shape to describe the velocity of the blood that flows into the vessel. As the inlet is a part of a long and straight blood vessel, it is assumed that $\vec{u_x} = \vec{u_y} = 0$. The first boundary condition also applies for the inlet and so $\vec{u} = \vec{0}$ at the vessel wall. As distance to the vessel walls increases, the velocity increases quadratically, resulting in a maximum velocity at the center of $\partial\Omega_{in}$ and a parabolic velocity profile over the rest of $\partial\Omega_{in}$:

$$\vec{u}(x,y,z) = (0,0,u_{inflow}(x,y)), \quad \text{for } (x,y,z) \in \partial\Omega_{in}. \tag{10}$$

In this equation $u_{inflow}(x,y)$ is a parabolic scalar function that is computed by SimVascular [31] in the following manner. Let $\partial\Omega_{in,outer}$ denote the outer rim of $\partial\Omega_{in}$. For every pair of opposite points inside $\partial\Omega_{in,outer}$, a parabolic function is fitted through them points (at which the $u = 0$) and the point at the center of the inlet. This process creates a function $u_{inflow}(V,x,y)$ for the velocity at every point in $\partial\Omega_{in}$, where on V, which denotes the velocity at the center of $\partial\Omega_{in}$. Then the equation

$$Q_{in} = \int_{\partial\Omega_{in}} u_{inflow}(V,x,y)\ \mathrm{d}x\ \mathrm{d}y$$

is solved to find V, where Q_{in} is an input parameter for the program that denotes the flow rate at the inlet.

The third boundary condition is applied at both outlets of the vessel shape to describe peripheral resistance, i.e. the resistance of the downstream vascular system to blood flow. This effect is modelled by a resistance $R = (70-160) \times 10^6\ Pa \cdot s/m^3$[17], that acts on the outlets of the mesh. The resistance is integrated into the model by applying it as an additional pressure p_{R1} at $\partial\Omega_{out,1}$ and p_{R2} at $\partial\Omega_{out,2}$, where $p_{R1} = RQ_1$ and $p_2 = RQ_2$. Here Q_1 and Q_2 are the flow rates through $\partial\Omega_{out,1}$ and $\partial\Omega_{out,2}$ respectively. In short, the third boundary condition is given by:

$$p(x,y,z) = p_0 + RQ_i, \quad \text{for } (x,y,z) \in \partial\Omega_{out,i}, \tag{11}$$

where p_0 is the atmospheric pressure that is the same everywhere in the vessel.
Using these boundary conditions along with the sequence of discretized variational forms derived in section 2.2, the flow profile can be found by iterating through time using the results of previous time steps. However, to start this process of iteration, an initial state is required. The initial conditions used in this study are:

$$\vec{u}(x,y,z) = \vec{0}, \quad \text{for } (x,y,z) \in \Omega$$
$$p(x,y,z) = 0, \quad \text{for } (x,y,z) \in \Omega.$$

3 Results

Simulations were performed in SimVascular and the visualization were made by ParaView [26], with flow rate $Q = 15000\ mm^3/s$, resistance value $R = 0.997g/mm^4 \cdot s$, density $\rho = 0.00106\ g/mm^3$ and dynamic viscosity $\mu = 0.004g/mm \cdot s$.

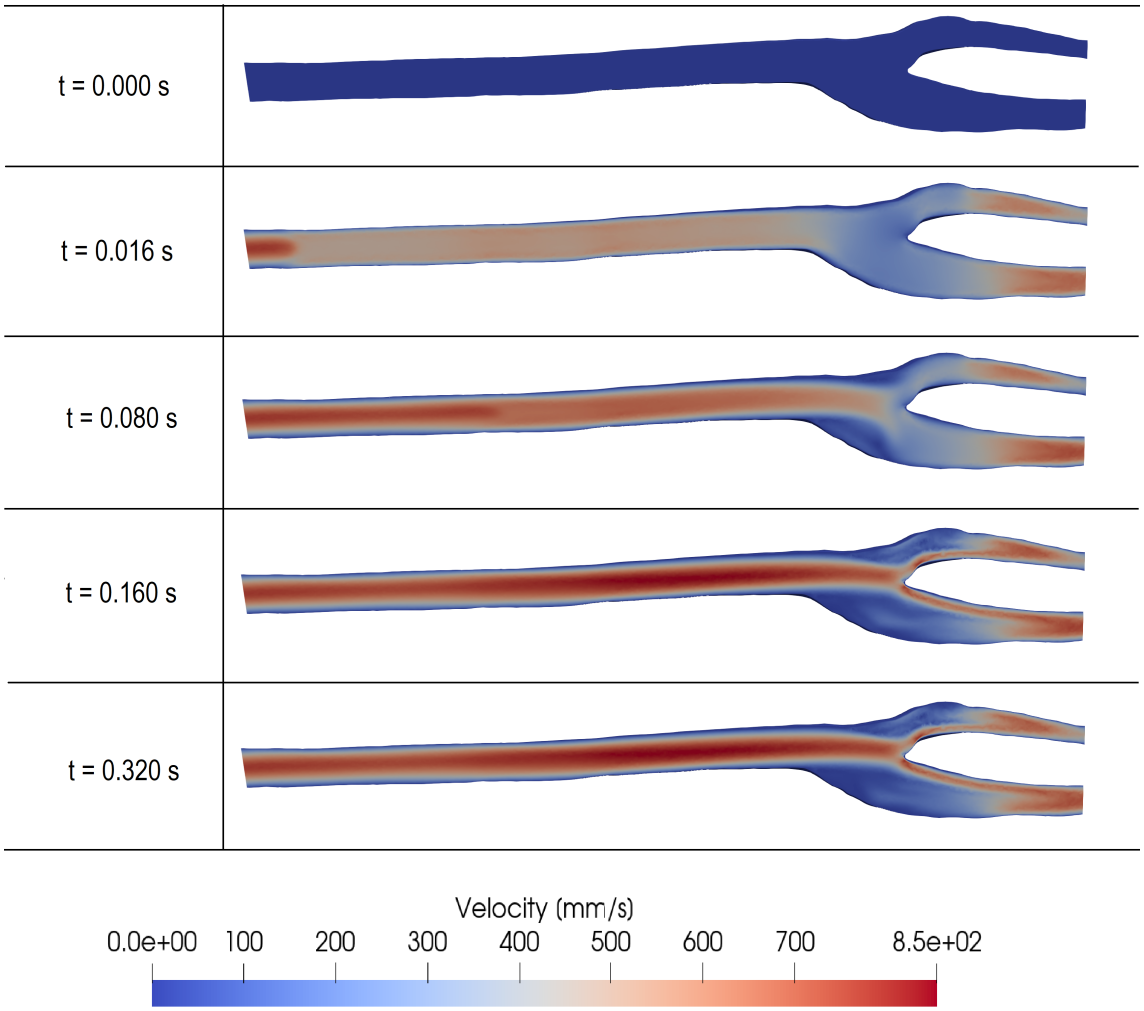

FIGURE 8: Velocity profile through the a central slice of the right carotid artery (absolute value), $\Delta t = 0.0004s$

Using the parabolic inflow defined in section 2.3, the velocity profile is initially high at the inlet and as time progresses the absolute value of the velocity increases at points further down the artery. After a certain amount of time t_{steady}, a steady state is reached and the flow profile is independent of time for all $t > t_{steady}$.
The simulations were run for different values of Δt, to check the convergence characteristics of the Krylov subspace solvers that SimVascular uses. For $\Delta t = 0.004\ s$, $t_{steady} \approx 0.19\ s$ and for $\Delta t = 0.005\ s$, $t_{steady} \approx 0.24\ s$. Thus, when a larger time step is used, it takes slightly longer for the steady state to be reached. Therefore it is favourable to use smaller time steps.

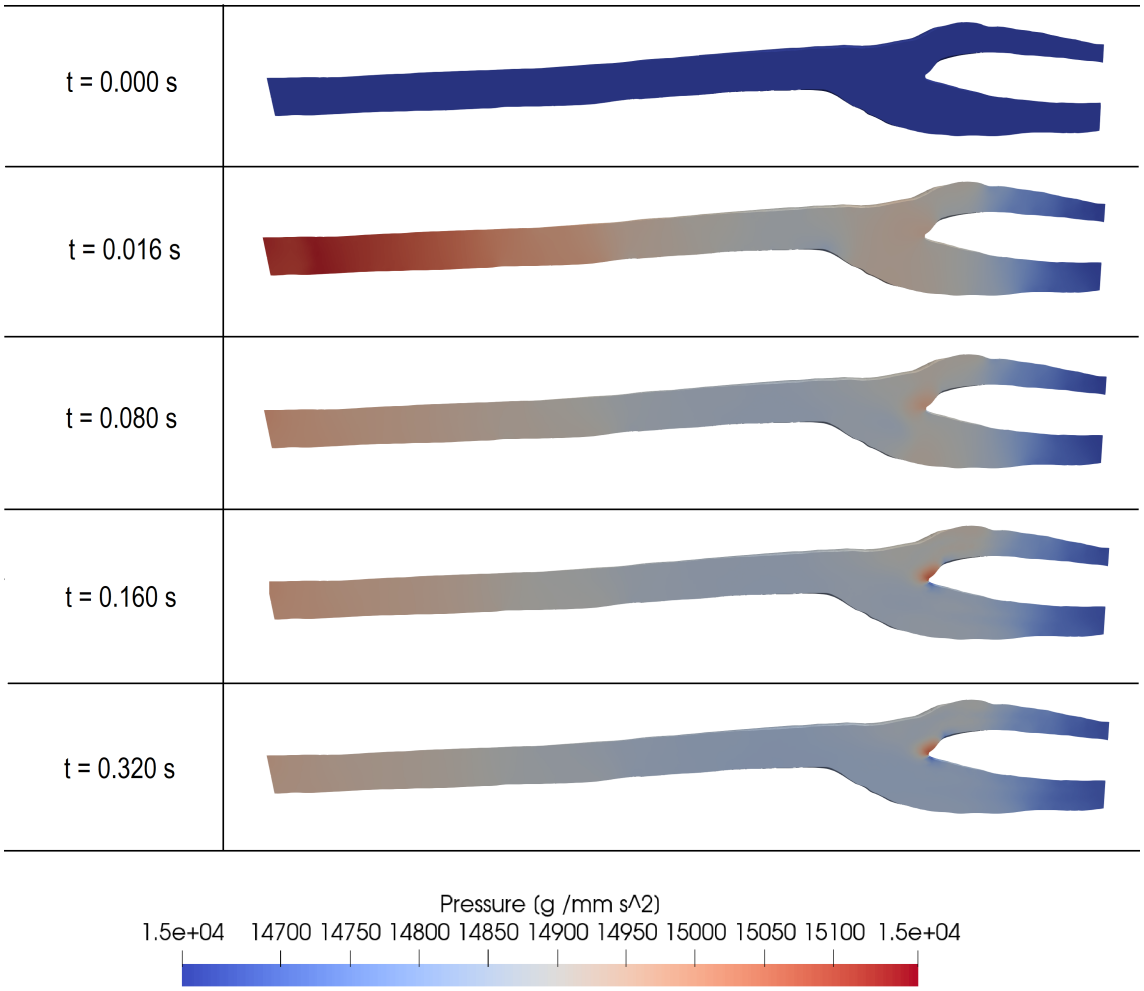

FIGURE 9: Pressure profile through the a central slice of the right carotid artery, $\Delta t = 0.0004\ s$

The pressure is initially high at the inflow as the blood that flows into the channel has to push the initially static blood through the channel. After the initial effects have worn off and the steady state is reached, the pressure is more evenly divided over the channel. In the steady state, a high amount of pressure is present at the bifurcation, this is due to the blood hitting the wall at a relatively high velocity as can be seen in Figure 8.

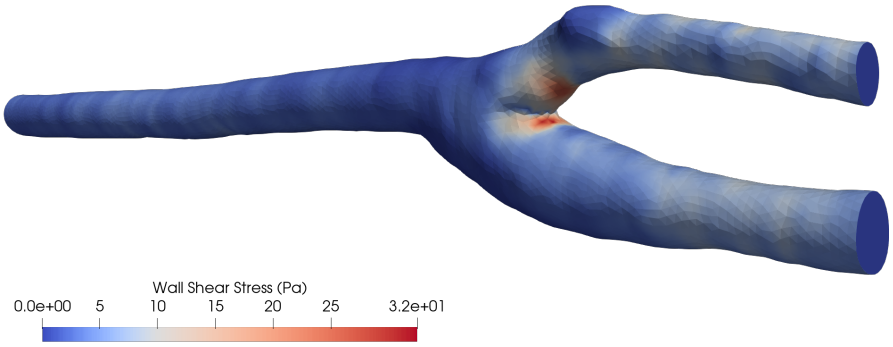

FIGURE 10: Wall shear stress profile through the a central slice of the right carotid artery for $t = 0.320\ s$, $\Delta t = 0.0004\ s$

Inside the common carotid artery, the wall shear stress is approximately constant. At the bifurcation however, the wall shear stress is significantly higher as the velocity of the blood that hits the bifurcation wall is higher than the velocity at the common carotid arterial walls. Additionally, the wall shear stress is very low at the opposite sides to the bifurcation as the blood velocity is relatively smaller there. The wall shear stress in the external and internal carotid artery is higher than the wall shear stress in the common carotid artery. This is due to the higher velocity of the blood and the smaller diameter of the vessel.

4 Discussion

In future studies, the 'rigid wall' assumption could be replaced by an elastic wall, and it could even be extended to include damping and longitudinal tension [11]. This is a way of improving the estimation of the WSS as a real vessel wall is also an active entity.
Another interesting improvement is to model the inlet boundary condition as a pulsatile flow, which is in closer resemblance of the actual flow pattern inside a blood vessel [21]. This way wall shear stress can be estimated over the entire cardiac cycle. This could be paired with an outlet boundary condition described by a resistance in series with a parallel capacitor and resistor as a way to describe the fluctuations in the peripheral resistance during different stages of the cardiac cycle [24]. This way, time averaged WSS could also be calculated.

A limitation to this model is also that the blood flow is modeled as a Newtonian fluid. While this is done in several other CFD studies, blood does show non-Newtonian behavior. Under steady flow conditions, differences in axial velocities and velocity gradients can be found between Newtonian and non-Newtonian blood flow simulations [13].
For the creation of the mesh, several alternatives are possible as mentioned in section 2.1. If one were to use the meshing procedure described in this study in future applications, the selection of which part of the vessel is usable for simulation and which part is regarded too noisy can be done based on a threshold on the uncertainty in the location of the segmentation algorithm. Additionally, to prevent that the bifurcation is overly smoothened, losing its shape characteristics, the remeshing can be based on the local curvature of the mesh. This way, the bifurcation still remains its shape, while the remaining part of the mesh is smoothened.
Finally, another approach to solving the sequence of variational forms in 2.2 is by using FEniCSx [17], which is an open-source computing platform for solving partial differential equations. It allows users to solve PDEs in an intuitive way, while still remaining control over over the flow modeling, which gives it an advantage over using SimVascular. However, due to technical issues and time constraints this study was unable to incorporate FEniCSx simulations. A GitLab link to a repository containing a currently non converging implementation of FEniCSx is provided: `https://gitlab.utwente.nl/mathematics-of-imaging-and-ai/bachelor-students/ties-martens.git`.

5 Conclusion

The method that was described, provides a method to describe blood flow inside a carotid arteries, based on data from MRI-derived carotid artery segmentations. The results in Figure 8 are both qualitatively and quantitatively similar to the result of other CFD studies[12]. The blood pressure in Figure 9is also similar to blood pressure measurements done in other studies [3]. However, while the WSS shown in Figure 10 is qualitatively similar to the WSS from another MRI-based CFD study, the WSS in this study is significantly higher. Variability in WSS estimation like this is common problem in this research area. In this case, the deviation might have to do with the fact that peak inflow and pressure are used in the model. Also, clinicians are usually not interested in the magnitude of the WSS stress, but rather in the qualitative development, therefore the WSS estimations could still prove to be useful in practice. In conclusion, this study provides a promising way of finding blood velocity and pressure inside the carotid arteries.

References

[1] Dieuwertje Alblas, Christoph Brune, and Jelmer M. Wolterink. In Olivier Colliot, Ivana Isgum, Bennett A. Landman, and Murray H. Loew, editors, *Medical Imaging 2022*, volume 12032 of *Progress in Biomedical Optics and Imaging - Proceedings of SPIE*. SPIE Press, April 2022. Funding Information: Jelmer M. Wolterink was supported by NWO domain Applied and Engineering Sciences VENI grant (18192). Publisher Copyright: © 2022 SPIE; Medical Imaging 2022: Physics of Medical Imaging ; Conference date: 21-03-2022 Through 27-03-2022.

[2] Hans Petter Langtangen Anders Logg and Jørgen S. Dokken. The navier-stokes equations. `https://jorgensd.github.io/dolfinx-tutorial/chapter2/navierstokes.html`, 2022. Accessed: 26 June 2022.

[3] Benjamin S Aribisala, Zoe Morris, Elizabeth Eadie, Avril Thomas, Alan Gow, Maria C Valdés Hernández, Natalie A Royle, Mark E Bastin, John Starr, Ian J Deary, and Joanna M Wardlaw. Blood pressure, internal carotid artery flow parameters, and Age-Related white matter hyperintensities. *Hypertension*, 63(5):1011–1018, 2014.

[4] G. Balarac, F. Basile, P. Bénard, F. Bordeu, J.-B. Chapelier, L. Cirrottola, G. Caumon, C. Dapogny, P. Frey, A. Froehly, G. Ghigliotti, R. Laraufie, G. Lartigue, C. Legentil, R. Mercier, V. Moureau, C. Nardoni, S. Pertant, and M. Zakari. Tetrahedral remeshing in the context of large-scale numerical simulation and high performance computing, 2021.

[5] Chirantan Banerjee and Marc I. Chimowitz. Stroke caused by atherosclerosis of the major intracranial arteries. *Circulation Research*, 120(3):502–513, 2017.

[6] Nicolas Buchmann and Mark Jermy. Particle image velocimetry measurements of blood flow in a modeled carotid artery bifurcation. *Proceedings of the 16th Australasian Fluid Mechanics Conference, 16AFMC*, 05 2007.

[7] Timothy A. Burkhart, David M. Andrews, and Cynthia E. Dunning. Finite element modeling mesh quality, energy balance and validation methods: A review with recommendations associated with the modeling of bone tissue. *Journal of Biomechanics*, 46(9):1477–1488, 2013.

[8] Paolo Cignoni, Marco Callieri, Massimiliano Corsini, Matteo Dellepiane, Fabio Ganovelli, Guido Ranzuglia, et al. Meshlab: an open-source mesh processing tool. In *Eurographics Italian chapter conference*, volume 2008, pages 129–136. Salerno, Italy, 2008.

[9] Michael Dawson-Haggerty. Trimesh, 2022.

[10] R Fitridge and M Thompson, editors. *Mechanisms of Vascular Disease: A Reference Book for Vascular Specialists*. University of Adelaide Press, 2011.

[11] L. Formaggia, J.F. Gerbeau, F. Nobile, and A. Quarteroni. On the coupling of 3d and 1d navier–stokes equations for flow problems in compliant vessels. *Computer Methods in Applied Mechanics and Engineering*, 191(6):561–582, 2001. Minisymposium on Methods for Flow Simulation and Modeling.

[12] Hamidreza Gharahi, Byron A Zambrano, David C Zhu, J Kevin DeMarco, and Seungik Baek. Computational fluid dynamic simulation of human carotid artery bifurcation based on anatomy and volumetric blood flow rate measured with magnetic resonance imaging. *Int. J. Adv. Eng. Sci. Appl. Math.*, 8(1):40–60, March 2016.

[13] F J Gijsen, F N van de Vosse, and J D Janssen. The influence of the non-newtonian properties of blood on the flow in large arteries: steady flow in a carotid bifurcation model. *J. Biomech.*, 32(6):601–608, June 1999.

[14] Katuhiko Goda. A multistep technique with implicit difference schemes for calculating two- or three-dimensional cavity flows. *Journal of Computational Physics*, 30(1):76–95, 1979.

[15] Amos Gropp, Lior Yariv, Niv Haim, Matan Atzmon, and Yaron Lipman. Implicit geometric regularization for learning shapes. *arXiv preprint arXiv:2002.10099*, 2020.

[16] Michael Kazhdan, Matthew Bolitho, and Hugues Hoppe. Poisson surface reconstruction. In *Proceedings of the fourth Eurographics symposium on Geometry processing*, volume 7, 2006.

[17] Mary E Klingensmith and Paul Wise. *The Washington manual of surgery.* Wolters Kluwer Health, Baltimore, MD, 8 edition, October 2019.

[18] Aoya Liu, Zhenqiu Yu, Ning Wang, and Wenhua Wang. Carotid atherosclerosis is associated with hypertension in a hospital-based retrospective cohort. *Int. J. Clin. Exp. Med.*, 8(11):21932–21938, November 2015.

[19] Pauline Marie Maietta. Accidental carotid artery catheterization during attempted central venous catheter placement: A case report. *AANA Journal*, 80(4):251–255, aug 2012.

[20] Michael Markl, Felix Wegent, Timo Zech, Simon Bauer, Christoph Strecker, Martin Schumacher, Cornelius Weiller, Jürgen Hennig, and Andreas Harloff. In vivo wall shear stress distribution in the carotid artery: effect of bifurcation geometry, internal carotid artery stenosis, and recanalization therapy. *Circ. Cardiovasc. Imaging*, 3(6):647–655, November 2010.

[21] Ian Marshall, Shunzhi Zhao, Panorea Papathanasopoulou, Peter Hoskins, and Yun Xu. MRI and CFD studies of pulsatile flow in healthy and stenosed carotid bifurcation models. *J. Biomech.*, 37(5):679–687, May 2004.

[22] N M Maurits, G E Loots, and A E P Veldman. The influence of vessel wall elasticity and peripheral resistance on the carotid artery flow wave form: a CFD model compared to in vivo ultrasound measurements. *J. Biomech.*, 40(2):427–436, 2007.

[23] Minh Tri Ngo, Chul In Kim, Jinmu Jung, Gyung Ho Chung, Dong Hwan Lee, and Hyo Sung Kwak. Four-dimensional flow magnetic resonance imaging for assessment of velocity magnitudes and flow patterns in the human carotid artery bifurcation: Comparison with computational fluid dynamics. *Diagnostics (Basel)*, 9(4), December 2019.

[24] Chen Peng, Junzhen Liu, Wei He, Wang Qin, Tong Yuan, Yuanqing Kan, Keqiang Wang, Shengzhang Wang, and Yun Shi. Numerical simulation in the abdominal aorta and the visceral arteries with or without stenosis based on 2d pcmri. *International Journal for Numerical Methods in Biomedical Engineering*, 38(3):e3569, 2022.

[25] Elizabeth V Ratchford and Natalie S Evans. Carotid artery disease. *Vasc. Med.*, 19(6):512–515, December 2014.

[26] William J Schroeder and Kenneth M Martin. Overview of visualization text and images taken with permission from the book the visualization toolkit: An Object-Oriented approach to 3D graphics, 3rd ed., published by kitware, inc. http://www.kitware.com/products/vtktextbook.html. In *Visualization Handbook*, pages 3–35. Elsevier, 2005.

[27] Hang Si. Tetgen, a delaunay-based quality tetrahedral mesh generator. *ACM Trans. Math. Softw.*, 41(2), feb 2015.

[28] Blausen.com staff. Medical gallery of blausen medical 2014. *WikiJournal of Medicine*, 1(2), aug 2014.

[29] Julian Suk, Pim de Haan, Phillip Lippe, Christoph Brune, and Jelmer M. Wolterink. Mesh convolutional neural networks for wall shear stress estimation in 3d artery models. volume 13131 LNCS, pages 93–102. Springer Science and Business Media Deutschland GmbH, 2022.

[30] Charles A. Taylor, Timothy A. Fonte, and James K. Min. Computational fluid dynamics applied to cardiac computed tomography for noninvasive quantification of fractional flow reserve: Scientific basis. *Journal of the American College of Cardiology*, 61:2233–2241, 6 2013.

[31] Adam Updegrove, Nathan M Wilson, Jameson Merkow, Hongzhi Lan, Alison L Marsden, and Shawn C Shadden. SimVascular: An open source pipeline for cardiovascular simulation. *Ann. Biomed. Eng.*, 45(3):525–541, March 2017.

[32] Sunčica Čanić, Andro Mikelić, Josip Tambača, Giovanna Guidoboni, Craig Hartley, Doreen Rosenstrauch, and Z. Krajcer. Fluid-structure interaction in blood flow. *Women in Mathematics*, pages 11–16, 2006.